Hierarchical whole-brain modeling of critical synchronization dynamics in human brains

Vladislav Myrov[a,1], Alina Suleimanova[a], Samanta Knapič[a,b], Paula Partanen[b], Maria Vesterinen[b], Wenya Liu[a,b], Satu Palva[b,c], and J. Matias Palva[a,b,c]

This manuscript was compiled on January 6, 2025

Brain activity exhibits critical-like dynamics, which is fundamental for cognitive functions. Whole-brain computational modeling has become indispensable in studying the systems-level mechanisms that govern the dynamics of large-scale brain activity in health and disease. However, previous approaches have focused on modeling either functional connectivity or criticality, and capturing both simultaneously in whole-brain systems remains a challenge. Here, we advance a new approach to modeling multi-scale synchronization dynamics with the Hierarchical Kuramoto model. At two levels of hierarchy, the model comprises a network of nodes that each encapsulate a large number of coupled oscillators, which enables dissection of local and inter-areal coupling and dynamics. We found the model to produce oscillations with critical-like dynamics, including emergent long-range temporal correlations (LRTCs) and inter-areal order correlations at the critical transition between asynchronous and synchronous phases. The model predicted unique structure-function relationships for functional observables so that coupling with structure peaked at criticality for LRTCs and order correlations but collapsed for inter-areal phase synchronization. Comparison of the model dynamics with human resting-state magnetoencephalography (MEG) showed that model-MEG correlations were maximized in the subcritical side of an extended critical regime for all observables and across the model parameter space. Finally, we found that the model may also yield realistic-like multi-peak power spectra and that also their similarity with MEG data is maximized below peak criticality. In conclusion, Hierarchical Kuramoto modeling yields realistic and separable local and global synchronization dynamics that are directly comparable with neuroimaging, which opens new avenues for understanding collectivity in brain activity.

Brain Oscillations | Criticality | Modeling | Kuramoto | MEG

Significance Statement

Healthy brain activity depends on both moderate levels of inter-areal phase synchronization and emergent critical-like dynamics. We introduce here the Hierarchical Kuramoto model that yields a novel framework for simulating both facets of critical synchronization dynamics on the whole-brain scale. The model revealed that the coupling between structure connectivity and emergent functional architecture has unique breakpoints for both synchronization and criticality. The similarity between emergent dynamics in the model and observed with magnetoencephalography systematically peaked on the subcritical side of an extended critical regime, suggesting that healthy brain activity *in vivo* is confined to this range. These findings provide a new platform of modeling whole-brain activity and accessing new mechanistic insight into the organizational principles of neuronal dynamics

Human brains *in vivo* exhibit moderate levels of long-range phase synchronization in both intra-cerebral stereo-EEG (SEEG) (1–3) and non-invasive M/EEG recordings (4–6). Synchronization plays mechanistic roles in regulating neuronal communication in brain networks (7–9) underlying cognitive functions (10–12). Inadequate or excessive synchronization, on the other hand, constitutes a core mechanism for neurological disorders such as epilepsy (2, 13) and Parkinson's disease (14), and characterizes neuropsychiatric diseases such as depression (15, 16), where abnormalities in synchrony are correlated with the severity of depressive symptoms (17–19).

Neuronal oscillations are rhythmic excitability fluctuations that arise with frequency-specific synaptic mechanisms in neuronal micro- and macrocircuits (20). To study these oscillations, researchers employ electrophysiological methods such as electroencephalography (EEG), stereo-EEG (SEEG), and/or magnetoencephalography (MEG) in humans (Figure 1A). Typically, recordings are collapsed into cortical parcellations, and the parcel time series are filtered to obtain narrow-band analytical time series (See Figure 1B). Observables such as local power spectra (See Figure 1C) that is a proxy to local neuronal synchronization within a population,and inter-areal amplitude (See Figure 1D,F) and phase correlations (See Figure 1E,G) to operationalize functional connectome, are then obtained.These measures of neuronal oscillations exhibit considerable variability in characteristics such as frequency, power, and inter-areal coupling (phase-synchronization, amplitude correlations) and this variability is functionally significant, e.g., in predicting cognitive performance (15, 21, 22), learning (23), and neurological state (13).

The framework of criticality provides an approach to understanding these neuronal dynamics and their variability: the "critical brain" hypothesis (24–27) proposes that the Operating Point (OP) of neuronal systems *in vivo* lies very near the critical phase transition between the subcritical (disorder) and supercritical (order)

Author affiliations: [a]Department of Neuroscience and Biomedical Engineering, Aalto University, Espoo, Finland; [b]euroscience Center, Helsinki Institute of Life Science, University of Helsinki, Helsinki, Finland; [c]Centre for Cognitive Neuroimaging, School of Neuroscience and Psychology, University of Glasgow, Glasgow, UK

V.M: conceived the study;model development;performed computational modeling;performed data analysis;
A.S.: performed computational modeling;performed data analysis;
S.K.: provided preprocessed DWI data;
P.P.: MEG data recording;
W.L.: provided preprocessed MEG data;
M.V.: MEG data recording;
S.P.: curated the data collection;
J.M.P.: conceived the study;

The authors declare no competing interests.

[1]To whom correspondence should be addressed. E-mail: vladislav.myrovaalto.fi

DRAFT

phases of the system's state space. Operation at critical transition leads to emergence of scale-free spatiotemporal correlations, observable both as long-range temporal correlations (LRTCs, (26)) and power-law scaled avalanches (27), and yields several functional advantages, such as maximized information capacity (24), complexity (28) and processing, dynamic range (29), and transmission rate (30, 31).

Operating point is a measure that defines the position in the system's critical state space. It is regulated by underlying control parameters that for neuronal systems are excitation-inhibition (E/I) balance (32), neuromodulation of synaptic plasticity (33, 34), and structural connectivity patterns such as network modularity (35–38). A given OP is associated with specific emergent dynamics, which can be operationalized with a range of synchronization and criticality observables (26, 27, 39–41). Because neither the control parameters nor the system's states are readily observable, their relationships with observables such as synchrony, LRTCs, and avalanches have remained a topic where computational modeling is essential for mechanistic understanding.

Numerous computational models have been developed to investigate the principles underlying whole-brain neural dynamics (42–44). Inter-areal functional connectivity (phase synchronization) has been modeled with the Wilson-Cowan model (3), Hopf model (45), and Kuramoto model (46–48).In contrast, computational models used in criticality research, have used to study avalanches using branching-process (49) and Ising models (50) from statistical physics, as well as neurophysiology-inspired population models (51–53) and networks of excitatory and inhibitory neurons (39) like the critical oscillations (CROS) model that exhibits LRTCs (54, 55).Thus, at present, there is a lack of models that would accurately capturate realistic oscillation-based functional connectivity and critical dynamics. The Kuramoto model is the simplest model of synchronization dynamics and captures the emergence of self-organized synchrony in a system of coupled oscillators. The model exhibits a transition between subcritical (asynchronous) and supercritical (synchronous) phases, characterized by the emergence of critical-like dynamics such as LRTCs (40) and avalanches (56). In prior research using Kuramoto modeling in the neuroscience context, the activity of the neuronal populations representing single cortical parcels has been represented by single Kuramoto oscillators (57). This approach models whole-brain network dynamics but does not yield criticality-relevant node-level observables such as order fluctuations or LRTCs. Another approach for using the Kuramoto model represents a neuronal system as either a single (58, 59) or two populations (48, 60) of oscillators, capturing critical-like dynamics at the node level but not extending the model into a whole-brain scale networks.

We advance here a hierarchical extension of the classic Kuramoto model, consisting of a whole-brain network where each node contains a large group of oscillators. This multi-level architecture yields separable local and inter-areal synchronization dynamics and allows direct comparability with neuroimaging data. Utilizing the model we investigated organizational principles in brain dynamics by examining the architecture of structural connections at different operating points, and compared the model output with MEG-observed dynamics. By further extending the modeling approach, we studied how multi-modal spectral properties behave at different levels of criticality. Ultimately, our approach enables whole-brain scale modeling of self-organized critical dynamics at both the nodal and systems levels, opening new avenues to investigate how system properties affect brain activity.

Results

Whole-brain model of critical oscillations. Activity in the brain is guided by interactions on both macro and micro scale from individual neurons to large neuronal populations whose magnetic fields are detectable with non-invasive neuromaging methods such as MEG (See Figure 1A). These complex interactions gives rise to oscillatory activity at different time-scales (See Figure 1B) and multiple phenomena are observed at inter- (See Figure 1C) and intra-areal levels (See Figure 1D-G).

In order to capture intra- and inter-areal dynamics simultaneously, we designed a hierarchical model in which each node is a full system of Kuramoto oscillators (20, 48, 61) analogous to each cortical area containing a large population of neurons. The oscillators are directionally coupled within the node with coupling weighted by local control parameter K (See Figure 1H, see Methods). We quantified within-node synchronization using the Kuramoto order, here refered as 'node order', defined as the alignment of oscillators' phases. Each node thus yielded synchronization dynamics with fluctuations between weaker and stronger internal synchronization (See Figure 1H) similar to the *in vivo* neocortical synchronization dynamics reflected in MEG oscillation amplitude fluctuations (See Figure 1B).

On the next level of hierarchy, we defined the interaction between the nodes as being guided by directional phase-difference of respective complex node time series weighted by node order and edge weight (see Methods). This approach encapsulates interactions between different levels of hierarchy and induces an additional level of heterogeneity in the model. We found that model time series exhibited local synchronization fluctuations (See Figure 1I) with both local features, such as power spectra (See Figure 1J), and inter-areal correlations, such as amplitude correlations (See Figure 1K,M) and phase synchrony (See Figure 1L,N), similar to those observed in real narrow-band MEG time-series.

Local and global control parameters shape the model critical-like dynamics. According to the critical brain hypothesis, neural networks operate near a critical point between order and disorder to optimize computational capabilities and adaptability. The state-space of critical dynamics emerges from a position in parameter space. In oscillatory network models, these parameters are local and global coupling strengths (Figure 2A) such that critical phase transition occurs between desynchronization and complete synchronization on both nodal and inter-node levels, operationalized with node order and inter-node phase synchronization, respectively. At the critical regime, oscillations are characterized by Long Range Temporal Correlations (LRTCs), operationalized using Detrended Fluctuation Analysis (DFA, See Figure 2B).

To assess how model parameters affect the criticality properties of the model, we set the initial distribution of inter-nodal edge weights to match a single-subject structural connectome (SC, quantified as DTI fiber count, see Methods).

DRAFT

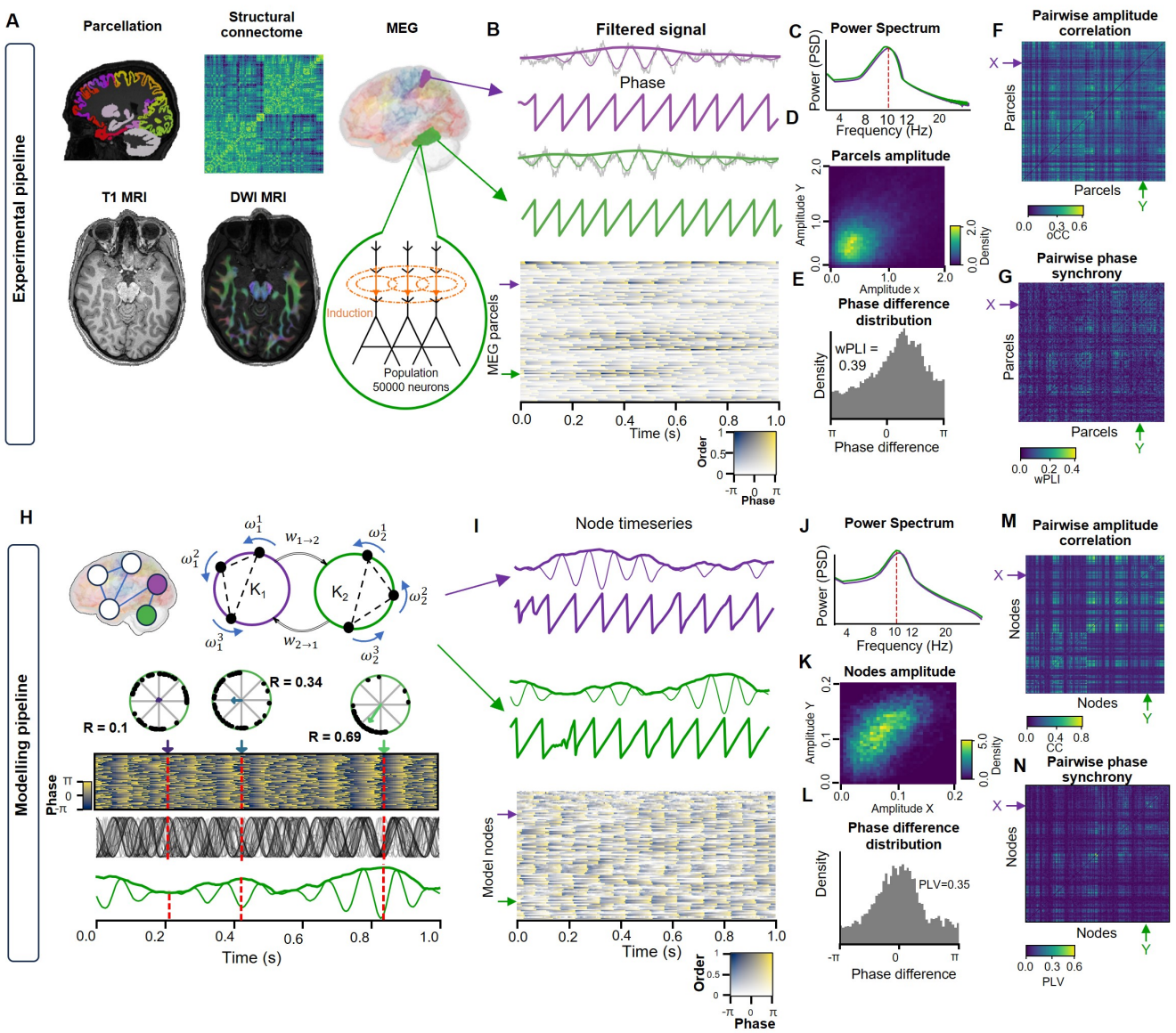

Fig. 1. General representation of an experimental pipeline. **A** Summary of imaging and data processing techniques, including T1-weighted MRI for anatomical parcellation, DWI MRI for structural connectome reconstruction, and MEG for functional data acquisition. The figure illustrates MRI-based parcellation, structural connectivity matrix, and MEG-derived population-level time series. **B** MEG signals from two parcels showing the broadband signal (gray) overlaid with the narrowband filtered component (10 Hz, Morlet wavelet, $\omega = 7.5$) and corresponding phase. Bottom: Phase heatmap of MEG signals across channels, with low-amplitude regions shown as transparent. **C** Power spectral density (PSD) for two parcels in the MEG data. **D** Two-dimensional histogram of amplitudes for two MEG signals filtered in the narrowband. **E** Distribution of phase differences between a pair of MEG signals, with a weighted phase lag index (wPLI) of 0.39. **F** Heatmap of pairwise amplitude correlations of alpha-band MEG signals (10Hz). **G** Pairwise wPLI matrix of alpha-band MEG signals (10 Hz). **modeling pipeline**. **H** On top level, the model is made of multiple inter-connected nodes where each node represents a single brain region. A node is comprised of huge amount (up to thousands) of basic Kuramoto oscillators with central frequency ω and intra-nodal coupling strength of K_n. The average value across oscillators is used to obtain complex timeseries **I** Simulated time series and corresponding phase for two model nodes. **J** Power spectral density of the real part of simulated time series. **K** Two-dimensional histogram of amplitudes for two simulated signals. **L** Phase difference distribution for two simulated signals, with an example PLV value of 0.35. **M** Pairwise amplitude correlation heatmap for simulated time series. **N** Pairwise PLV matrix of simulated signals.

We then simulated resting-state activity (see Methods) and computed the DFA exponent for each channel of the simulated time series as a function of the local coupling coefficient (K) and global coupling coefficient (L).

The hierarchical approach effectively modeled the critical transition, and this transition featured a peak in the DFA scaling exponent near 1, indicating critical-like dynamics (See Figure 2C). Interestingly, the position of the DFA exponent peaks in the control parameter space vary between model nodes, indicating inter-node variability that could be caused by differences in node-level parameters.

Next, we created a cohort of structural-connectome-informed models ($N = 24$) and analyzed the behaviour of intra- and inter-node level observables. At the nodal level, we found that DFA exponent peaks during the phase transition of node order and the breakpoint aligns with maximum criticality (See Figure 2D). It is worth noting, that inter-subject variance emerges in slightly subcritical region

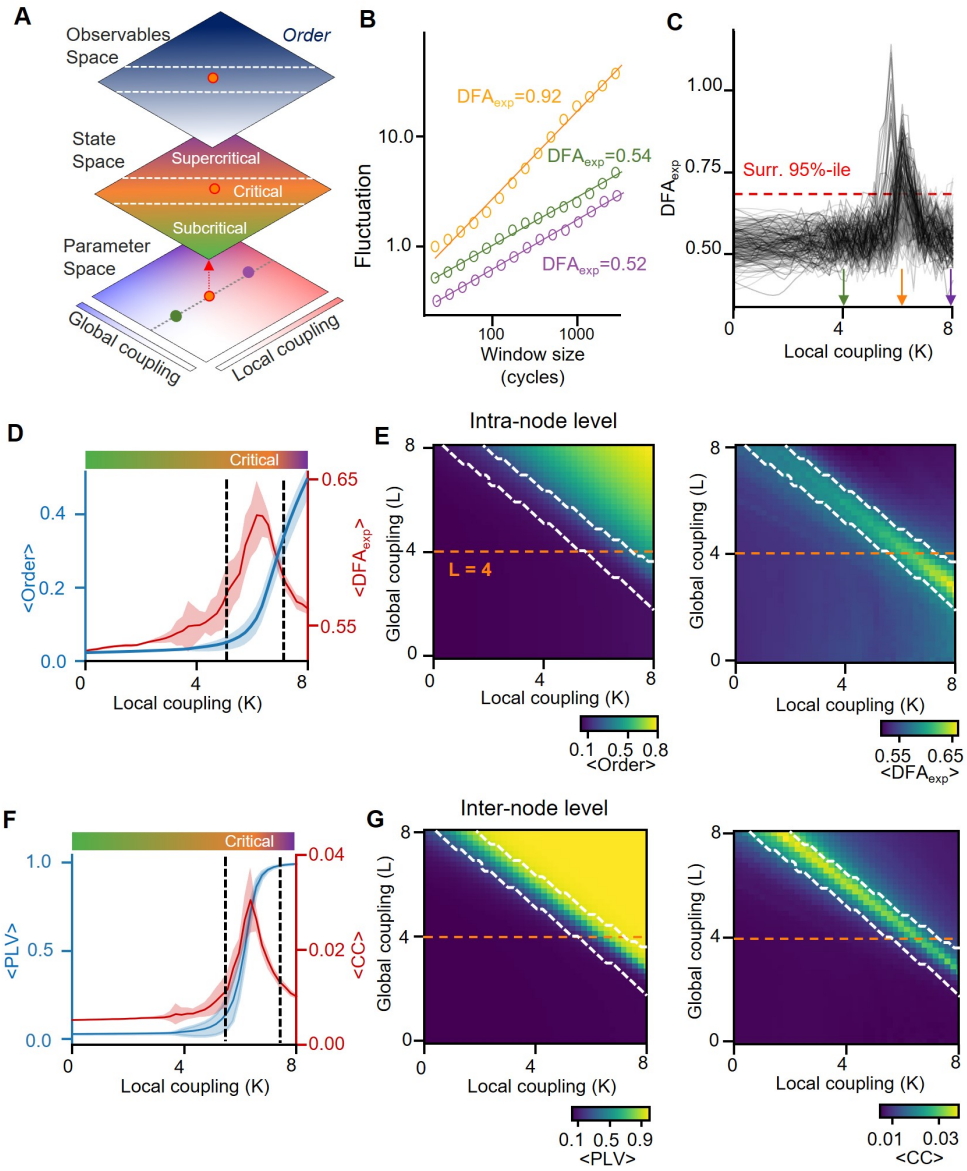

Fig. 2. Phase transition and emergence of critical-like dynamics in Hierachical Kuramoto Model. **A** Simplified representation of the parameter space, illustrating two key control parameters: local coupling strength (K) and global coupling strength (L). Colored dots indicate three distinct parameter combinations representing subcritical, critical, and supercritical regimes. **B** Example time series for subcritical, critical, and supercritical dynamics, corresponding to the parameter combinations in **A**. Right: Detrended Fluctuation Analysis (DFA) fits and their exponents (DFA_{exp}) for each regime. **C** DFA exponent (DFA_{exp}) as a function of local coupling strength (K), where each line represents a single model node. Black lines indicate nodes with significant DFA_{exp} peaks ($DFA_{exp} \geq 0.65$), while gray lines represent nodes without significant peaks. The red dashed line marks the significance threshold. **D** Average model order (blue) and DFA_{exp} (red) as a function of local coupling strength (K). The critical regime (shaded) is defined as the region where more than 10% of nodes exhibit $DFA_{exp} > 0.65$. Shaded areas represent standard error (SE) confidence intervals ($\pm \frac{SD}{\sqrt{N}}$, where $N = 24$ models). **E** Heatmaps of average order (left) and DFA_{exp} (right) across model nodes as functions of local (K) and global (L) coupling strengths. The white contour outlines the critical regime, defined as regions where more than 10% of nodes have $DFA_{exp} > 0.65$. **F** Average Phase Locking Value (PLV, blue) and cross-correlation (CC, red) as functions of local coupling strength (K). **I** Heatmaps of PLV (left) and CC (right) averaged across inter-nodal edges, as functions of local (K) and global (L) coupling strengths.

before the critical-like zone and also achieves a maximum at criticality. On the KL surface – the DFA exponent as a function of both control parameters – the critical region is represented by a linear ridge and achieves a maximum when local coupling is a bit lower than global (See Figure 2E).

Inter-nodal interaction dynamics showed a transition from near zero synchronization to almost perfect synchrony, the cross-correlation peaking during the transition period and matches the critical region assessed with LRTCS (See Figure 2F,G). Unlike the DFA exponent which is maximized when $K > L$, the cross-correlation achives the highest values when $L > K$.

Similar results were reproduced with a log-transformed structural connectome (see Supplementary Figure 1), however, the variability between critical peaks is lower and the critical ridge is more narrow in contrast to the original non-transformed SC. Consequently, the average DFA exponent and CC are higher when using log-transformed edge weights. This highlights that the emergence of LRTCs is not a

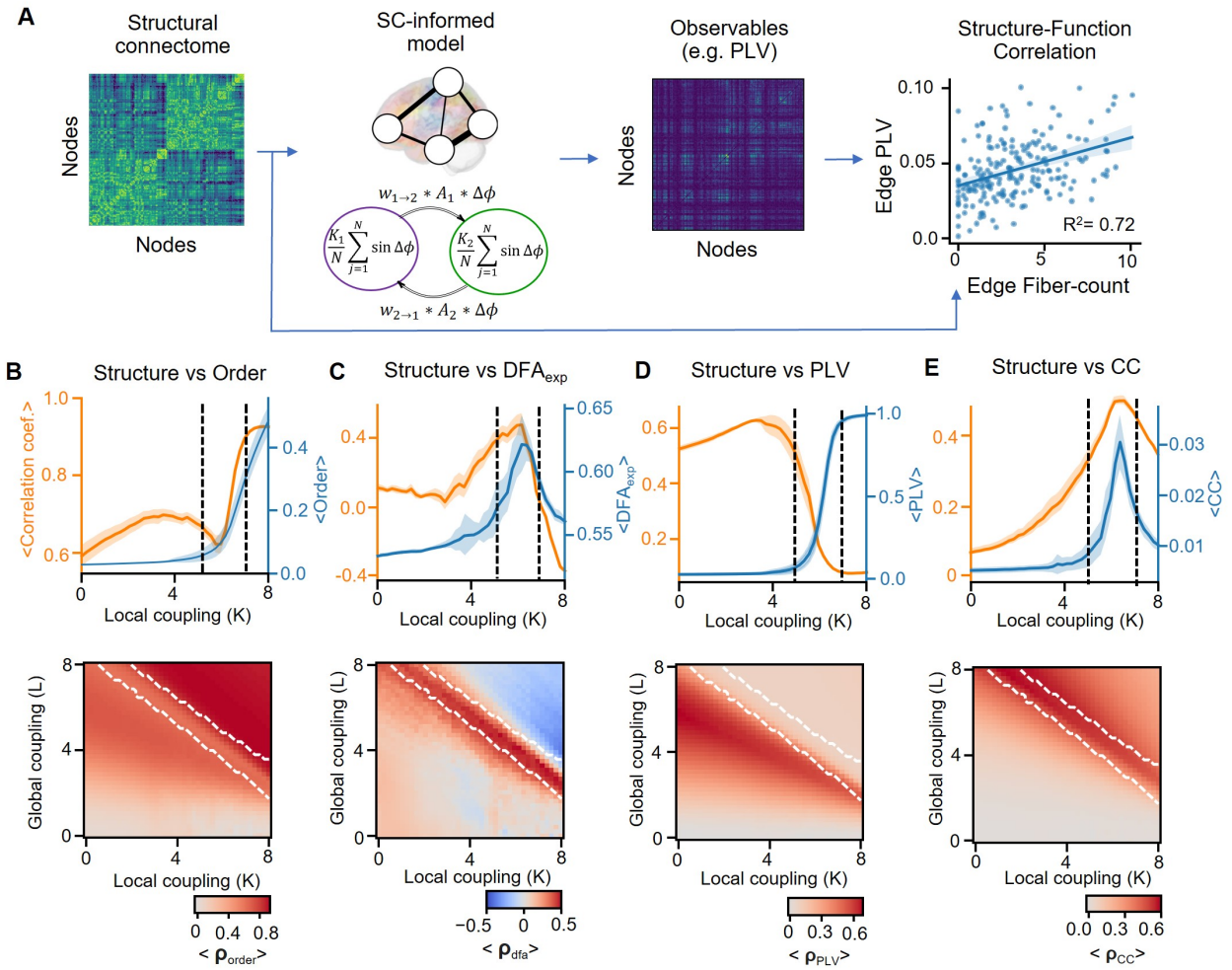

Fig. 3. Modeling reveals diverse forms of Structure-Function coupling around the phase transition. **A** Analysis pipeline: The structural connectome (SC) of an individual is used to construct an SC-informed Kuramoto model, where inter-nodal coupling weights are derived from the SC. The model generates oscillatory dynamics, from which observables such as Phase Locking Value (PLV), DFA exponent (DFA_{exp}), order, and amplitude cross-correlation (CC) are computed. Structure-function coupling is quantified as the correlation between these observables and structural measures (e.g., node strength or edge fiber count).**B-E** Correlation between model order and SC node strength (**B**), DFA_{exp} and SC node strength (**C**), PLV and SC edge weight (**D**), node order cross-correlation and edge weight (**E**) as a function of local coupling strength (K). Orange line indicates Pearson correlation coefficient (ρ) and the blue line average observable. Shaded areas represent confidence intervals (CIs) based on standard error (SE). On the bottom, heatmaps showing the Pearson correlation coefficient between the respective observables and structural measures (node strength or edge strength) as functions of local (K) and global (L) coupling strengths. The white contour outlines the critical regime consistent with Figure 2.

property of a specific structural architecture but is a general phenomena.

Interaction-specific breakdown or maximization of structure–function coupling at criticality. The structural connectome is a backbone of functional relations in the brain and despite there were numerous studies assessing their relations, criticality was not taken into account. To analyze relationships between the model's structural architecture and oscillatory dynamics, we computed the Pearson correlation coefficient using prior simulations. We correlated node strength (average structural connectivity of a node) with node-level observables (e.g., order, DFA exponent), and inter-node statistics (e.g., edge strength of PLV/CC) were correlated with edge weights (Figure 3A).

Investigating the structure-function correlations in the model at the individual node level, we found that the node order was positively correlated with Node Strength (NS, average edge weight of each node), increasing slightly from the subcritical to the critical region, dipping at criticality, and increasing sharply at supercritical region (See Figure 3B). Notably, this correlation remains around zero independent of the local coupling in a region with low but non-zero global coupling parameter (See Figure 3C).

The correlation between the DFA exponent and NS, on the other hand, fluctuates around zero in the subcritical region, peaking at criticality, and becoming strongly negative in the supercritical zone (See Figure 3D). A similar phenomenon was observed on the KL surface when DFA-structure correlation was maximized at the critical region (See Figure 3E).

At the inter-node level, the correlation between edge strength and CC resembled the patterns observed with the DFA exponent, peaking at criticality while remaining low in both subcritical and supercritical zones (See Figure 3H,I). The correlation between PLV and edge strength exhibited a

unimodal shape, with a wide peak on the subcritical side and dropping around the critical peak (See Figure 3F). Unlike other observables, the PLV showed higher correlation with SC in regions where global coupling is stronger than local coupling (See Figure 3G).

As a result we found that the correlation between the model structural properties explains observed oscillatory dynamics differently for synchronization and criticality properties. The correlation between edge weights and intra/inter-areal synchronization dips in the critical region but peaks for LRTCs and cross-correlation. Given these results we hypothesize that synchronization will be the most sensitive to internally-caused changed in coupling strength (e.g. plasticity-induced) or external perturbation such as stimuli in subcritical system while LRTCs and cross-correlation will require fewer changes to control at criticality.

Brain dynamics during the resting-state is the most correlated with observables in subcritical-critical region. The model demonstrates a wide spectrum of self-organized dynamics from sub-critical to critical regimes, and we asked how similar is the model activity to that observed in human resting-state MEG recordings. Narrow-band MEG signals were derived by filtering broad-band MEG resting-state recordings from 24 subjects using Morlet wavelets ($\omega = 7.5$). Frequencies ranged logarithmically from 2 Hz to 100 Hz across 41 bands. From these signals, we computed key observables of oscillatory dynamics, including the weighted Phase Lag Index (wPLI), DFA exponents, and amplitude cross-correlation (Figure 4A). For wPLI and CC we also included in the analysis the average value across edges that belong to the same node.

Next, we developed a structural connectome (SC)-informed model by initializing inter-node coupling strengths based on an averaged structural connectome across subjects. For simulated data we computed DFA exponents, PLV and CC (both node and edge-level), and for MEG data we computed the same observables but wPLI instead of PLV (See Figure 4B). Finally, to evaluate the similarity between real MEG recordings and simulated data, we estimated Pearson's correlation coefficients between observables from model nodes/edges and MEG parcels/edges corresponding to the same anatomical regions.

As a starting step, we analyzed the similarity between model and MEG dynamics as a function of narrow-band frequency. The model showed the most similar dynamics to the low-frequency activity, particularly in the theta frequency range (3–8Hz) for the DFA exponent and node- and edge-level phase-synchrony. However, the amplitude correlation exhibited several significant peaks including theta (4.2Hz), alpha (12.3Hz) and beta frequencies (28.3Hz, See Figure 4C).

Investigating the most-similar frequencies, we found that the significant correlation for all observables included in the analysis was found following the critical ridge (See Figure 4D-H), which supports the notion that the human brain operates primarily in a subcritical-critical zone. Interestingly, the correlation coefficient for the DFA exponent and node-level CC is positive on the subcritical side of the critical regime but becomes negative on the critical-supercritical side (See Figure 4D,F) which may indicate that the critical region in the human brain might be wider than observed in the model.

The spectral properties of oscillatory activity are shaped by the distribution of underlying frequencies. Traditionally, oscillations are quantified by their magnitude, often using power spectral methods. Different system properties, such as interaction delays, have been shown to regulate the shape of the spectra and emergence of oscillatory modes. However, in previous studies, the operating point of a system was not considered.

To replicate individual power spectral properties in the model, we aligned the oscillator frequency distribution with the shape of the recorded power spectrum. We achieved this by first computing the power spectrum density (PSD) of the MEG recordings and removing the 1/f component using the FOOOF method (62). The resulting PSD was then transformed into a probability distribution of oscillator frequencies by normalizing it with the cumulative sum. For each model node, we sampled brain-region oscillator frequencies from these distributions individually for each MEG parcel (Figure 5A).

To assess the similarity between real and simulated data, we computed the PSD of the simulated and MEG data using the Welch method, and estimated the Pearson correlation coefficient between them. In addition, we estimated the model frequency shift calculated by the absolute distance between alpha peaks in model and MEG spectra.

Initially, we found that regions with low intra-nodal coupling and high inter-nodal coupling in the subcritical side showed low, non-significant peaks in the power spectrum. In the supercritical model, a dominant peak appeared in the power spectra at the alpha band. Additionally, the power spectrum exhibited a slight drift toward the weighted average of alpha (9.8 Hz) and beta (19.5 Hz) frequencies, calculated as 12.85 Hz weighted by frequency probability. In contrast, the spectrum of the critical-like model was well-matched, with the peaks corresponding to those observed in the real data (See Figure 5B).

Since the properties of critical-like dynamics—particularly the critical state's position within the control parameter space—depend on the oscillator frequency distribution, we initially investigated whether a model with a heterogeneous non-parametric frequency distribution exhibits such dynamics. Our findings confirm that a model initialized with a non-parametric distribution of oscillator frequencies does indeed display critical-like dynamics and LRTCs emerge during the phase transition at the same time preserving the multi-frequency activity (see Supplementary Figure 3).

Analyzing the similarity between the model and the MEG-derived power spectrum, we found that the highest correlation was achieved on the subcritical side of the extended critical regime, with high local and low global coupling strength and it decays after the critical ridge where the alpha frequency becomes the driving force (See Figure 5C,D).

As the model transitioned from the subcritical to the critical regime, oscillatory peaks began to emerge. These peaks, largely absent at low control parameters, grew with increasing coupling strength and became dominated by the alpha band near the critical zone. Interestingly, the peaks were well-aligned with the real data in the subcritical and critical states, but in the supercritical regime, the alpha and beta frequency peaks exhibited a small drift toward the weighted average. The low correlation between the simulated

DRAFT

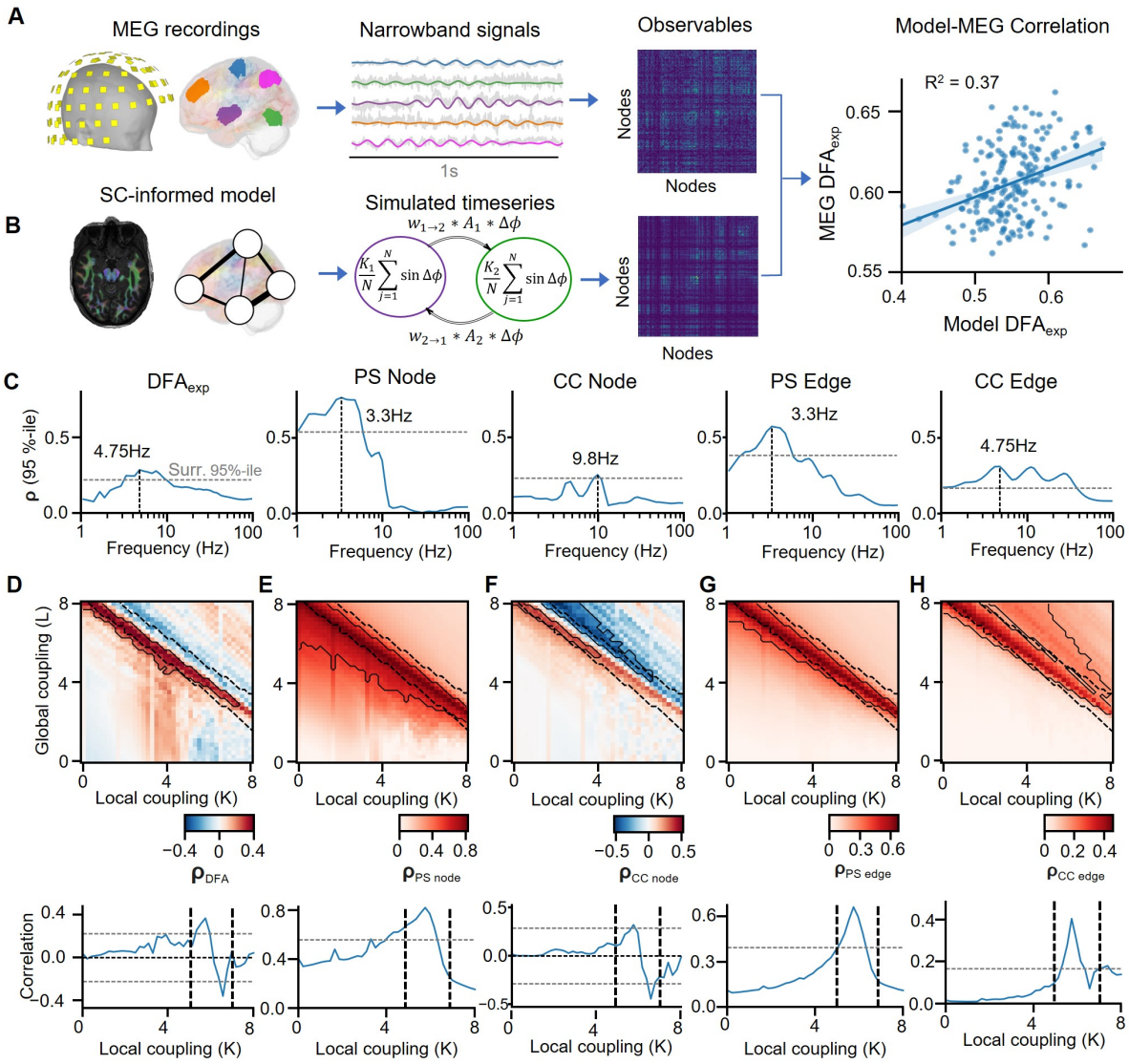

Fig. 4. The model observables on the subcritical slope of the Griffiths Phase are the most similar to those found in MEG recordings. A. MEG analysis pipeline: MEG recordings are source-modeled to derive parcel-level time series, filtered into narrowband signals (e.g., using Morlet wavelets), and analyzed to compute observables such as phase synchronization matrices. **B** Modeling pipeline: The SC-informed Kuramoto model is used to simulate time series, from which the same observables (e.g., phase synchrony, DFA exponent) as in MEG data are computed. Pearson correlations are calculated between MEG and model observables at the parcel (node) level to quantify structure-function similarity. **C** The 95th percentile of the Pearson correlation coefficient across the KL-surface between MEG and model observables as a function of frequency. The dashed horizontal line indicates the statistical significance threshold determined via spin-permutation tests. The vertical dashed line highlights the frequency at which the correlation peaks. **D-H** Correlation maps and KL-surface slices for observables at the peak frequency identified in **C**. The Pearson correlation coefficient between simulated and MEG-derived DFA exponent (**E**), average phase-synchrony of a node (**D**), average cross-correlation of a node (**F**, edge phase synchrony (**G**) and edge cross-correlation (**H**) as a function of local (K) and global (L) coupling coefficients for frequency with maximum 95th percentile (see **C**). Black thick contours in the heatmaps indicate regions with statistically significant correlations ($p < 0.01$) based on spin-permutation tests. Black dashed contours delineate the critical regime (as defined in Figure 2). The line plots at the bottom represent a slice of the KL-surface for the same L = 4.

and real data could be explained by this drift in the power spectrum properties (See Figure 5E).

These findings suggest that operating near criticality achieves a precise balance in spectral properties. This balance enables the model to generate significant peaks in the power spectrum, closely reproduce MEG-derived PSDs, and prevent collapse into a singular frequency maintaining a bimodal spectrum.

Discussion

Neuronal oscillations are fundamental to brain function and exhibit significant inter-areal and inter-individual variability in synchronization dynamics. Computational modeling approaches are emerging as central tools for understanding the systems-level mechanisms that determine the local and inter-areal synchronization dynamics of neuronal oscillations in brain health and disease.

This study presents a whole-brain-scale Hierarchical Kuramoto network model, which replicates key features of *in vivo* human brain dynamics and generates novel, experimentally

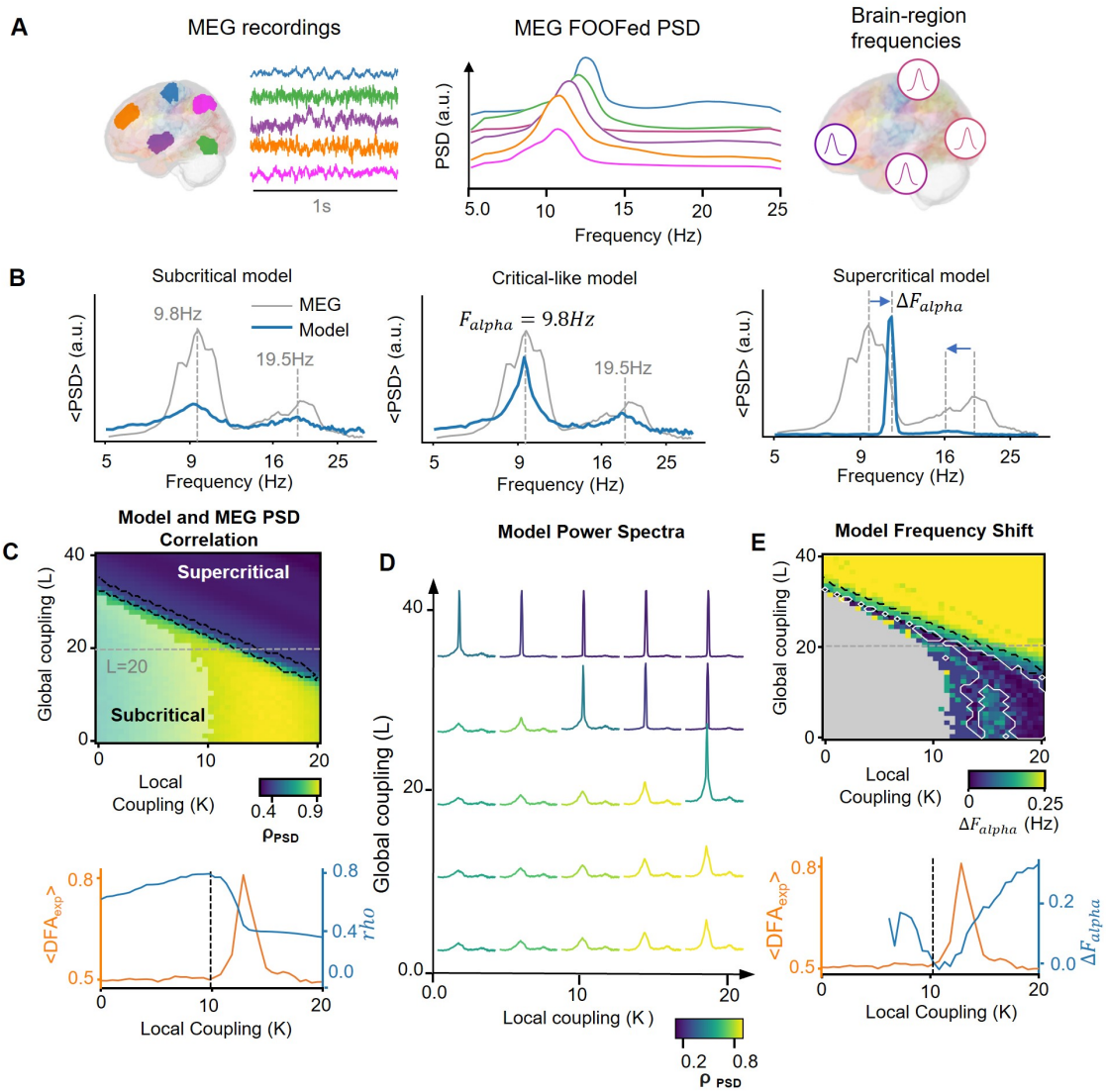

Fig. 5. Critical-like state supports multi-frequency spectral properties A Oscillator frequency distribution derived from parcel-level power spectral density (PSD) of real MEG recordings (left panel), with the $1/f$ component subtracted (middle panel) and are individually set for mode node that corresponds a brain area (right panel). **B** Average PSD across model nodes (blue) compared with MEG-derived PSD (gray) for three regimes: subcritical, critical, and supercritical. Dashed vertical lines indicate the alpha (∼9.8 Hz) and beta (∼19.5 Hz) frequency peaks. The critical model aligns closely with MEG-derived PSD, while subcritical and supercritical regimes deviate. **C** Pearson correlation coefficient between MEG-derived and simulated PSDs as a function of local (K) and global (L) coupling strengths (upper panel). The black contour highlights the critical ridge, defined by DFA exponent ($DFA_{exp} \geq 0.65$). The semi-transparent area indicates regions without significant spectral peaks. Bottom panel: Correlation coefficient (orange) and average DFA_{exp} (blue) as functions of local coupling (K) for a fixed global coupling (L = 20). **D**Model PSDs for different combinations of local (K) and global (L) coupling strengths, color-coded by their correlation with MEG-derived PSDs, as shown in **C**. Simulated spectra with critical-like dynamics exhibit the most realistic multi-peak structure. **E**. Difference between simulated and MEG alpha peak frequencies (ΔF_{alpha}) averaged across model nodes as a function of control parameters. The white contour highlights regions with significant alignment of alpha peaks. Bottom panel: ΔF_{alpha} (orange) and average DFA_{exp} (blue) as functions of local coupling (K), indicating the region of optimal alpha frequency alignment with critical-like dynamics.

testable predictions. Each node in the model represents a meso-scale neuronal population, encapsulated by a large ensemble of Kuramoto oscillators corresponding to cortical parcels and subcortical regions. As established in prior art of whole-brain model studies, these nodes are then connected into a whole-brain network with coupling that is proportional to the counts of individual white-matter axonal fibers connecting each parcel pair (See Figure 1). This approach enables realistic local synchronization dynamics and cortical heterogeneity in a manner that are directly comparable with experimental data and provides insight into whole-system dynamics. In particular, the nodes in the Hierarchical Kuramoto model reproduce several features of critical meso-scale brain dynamics observed in electrophysiological recordings, such as LRTCs in amplitude dynamics, power spectra, and rhythmicity (2, 40, 59, 63). Moreover, while Kuramoto models express phase correlations by design, we found the model to also express *in vivo*-like (2, 5, 21) emergent amplitude correlations, i.e., inter-areal correlations in local synchronization dynamics.

We found that these distinct brain dynamics observables exhibited unique structure-function relationships across the

critical phase transition. Here, we elucidated the models predictions for the unique structure-function coupling of different functional observables across the state space. We further assessed the similarity of the model's inter-areal correlation structures with those observed in MEG data and found results that strongly suggest human brains operate on the subcritical side of an extended critical regime. Importantly, the model is computationally highly efficient and enables simulations at the level of millions of interacting individual oscillators.

A wide range of computational models has been developed to study emergent brain dynamics at scales ranging from cell population approaches, such as the CROS model (39), to large-scale mean-field models, like the Wilson-Cowan (64), and to models utilizing oscillators to represent brain regions such as the Kuramoto (45, 61) or the Hopf (52) model. In this work, we extended this approach by introducing a hierarchical model, where a single node encapsulates a population of individual oscillators. Governed by the complex non-linear interaction between these oscillators, the model allows to reconstruct local and global critical-like dynamics simultaneously with emergence of powerlaw long-range temporal correlations on node-level and amplitude cross-correlation on inter-nodal level.

The "critical brain" hypothesis suggests that the brain operates near a phase transition between order and disorder, where critical dynamics emerge (24, 25). Notably, long-range temporal correlations (LRTCs, (40, 41, 65)) and avalanche dynamics (41, 66, 67) emerge during phase transition, which are key signatures of critical-like dynamics. The model effectively captured the expected phase transition, demonstrating low inter-areal phase synchronization and local order in the subcritical phase, which increased toward complete synchronization in the supercritical phase (40, 68).

At criticality, such phase-based measures of order thus exhibit moderate values, which magnitude match well with in vivo research that invariably reports neuronal synchronization to be weak to moderate. In the model, we observed that the dynamics of inter-node synchronization as a function of local coupling have a sigmoidal shape and start to grow in the subcritical regime and achieve PLV of ~ 0.35 at criticality. In contrast, local synchronization remains low ($\sim 0.05 - -0.1$) at critical point and starts growing rapidly afterwards. In addition, the variability in observables emerges around criticality and vanishes at supercritical state.

While intra- and inter-areal synchronization was maximuzed by minimization of zero-lag phase difference, node-order correlations at the whole-brain level peaked at criticality, similar to LRTCs. This is congruent with a prior study reporting maximal amplitude correlations at criticality among spiking-neuron networks in a two-node system (54). Notably, the amplitude correlations emerge in the model without direct optimization but as a result of concurrent changes in local synchronization. In the bigger picture, we propose that amplitude correlations in oscillatory systems are analogous to power-law dynamic correlations (32) that emerge at criticality in models of physical systems, such as the Ising model. In the context of complex oscillatory critical-like systems such as the brain, we hypothesize that the information transfer is maximized at criticality.

Recent studies have shown that the architecture of inter-nodal connectivity shapes the criticality properties, and a localized, highly-modular topology gives rise to oscillatory dynamics with long-range temporal correlations (37, 69, 70). Furthermore, alterations in connectivity push the system out of criticality towards a subcritical state (71). However, the nature of the structure-function relations at different critical-like states remains unknown.

Analyzing the structure-function relationships in the model, we found that the magnitude of linear correlations between the model's structural connectivity and observables of oscillatory dynamics was dictated by the model's operating point. The inter- and intra-areal synchronization had the strongest correlation with structural connectome in the subcritical region and linear structure-function relationship broke down at criticality. On the other hand, the correlation of inter-areal amplitude correlations and DFA exponent with structural connectivity peaked at criticality and vanished in both sub- and supercritical phases.

The brain criticality framework posits that a brain operates at the phase transition which was shown on microcircuit level (72). On a whole-brain scale level in humans, it was shown that models tuned to criticality (73, 74) and models operating in the region of metastability (45, 75) achieves the highest correlation with functional connectivity in MEG and fMRI recordings. But physiological plausibility of other observables and expecially several of them simultaneously has remained *terra incognita*.

In this study, we extended the research and included LRTCs and cross-correlation to the palette of observables. We found that the highest correlation between simulated and MEG-derived observables is achieved on the subcritical slope of the critical regime – not at its peak. Furthermore, the correlation between signatures of critical-like dynamics, such as the DFA exponent and order cross-correlation, was negative on the supercritical side of the critical regime. This finding suggests that the critical regime in human brains may be wider than what is observed in the model.

The power spectrum is one of the fundamental methods to investigate and operationalize oscillations and prior studies have suggested multiple mechanistical principles underlying power spectrum properties. On a neuronal-population level the hybrid models has achieved a great success with mimicing the individual spectral properties (76), and on a macro-scale it was revealed that physiologically plausable power spectrum is observed within the critical region of high metastability (45).

Here, we show that the PSD shape is defined by the both distribution of underlying oscillators frequencies and the position in the critical space. We found that the model is able to reproduce the spectral characteristics with the highest correlation between simulated and MEG power spectra around the subcritical side of the extended critical regime with high local and low global control parameters. Varying these parameters changes the rhythmic properties from an almost complete absence of oscillations in the subcritical region to strong, sustained oscillations with peaks shifted towards the weighted average of the oscillator frequencies. Based on these results, we hypothesize that activity in the critical-like region achieves a balance between sustained oscillations with persistent individual peaks without collapsing into a singular central frequency.

DRAFT

In conclusion, we introduce here a framework for generative hierarchical models of synchronization dynamics that enable explicit representation of local and inter-areal coupling and observations of emergent multi-scale synchronization dynamics. Our results show that the Hierarchical Kuramoto model produces meso- and macro-scale synchronization-dynamics observables that are physiologically plausible in the light of MEG data. The model enables detailed analysis of control parameters for local and inter-areal coupling, paving the way for future studies on personalized modeling of stimuli responses.

Materials and Methods

Hierachical kuramoto model. The classical Kuramoto model describes the synchronization dynamics of coupled oscillators, where each oscillator aligns its phase with others based on coupling strength

$\frac{\delta\phi_i}{\delta t} = \omega_i + \frac{1}{N}\sum_{j=1}^{N} K_{ij} sin(\phi_j - \phi_i)$

where N is the total number of oscillators, ϕ_i is the i-th oscillator phase, ω_i is the frequency of the i-th oscillator and K_{ij} is the coupling parameter between the i-th and j-th oscillators.

In this framework, each oscillator represents a brain region or parcel, and the coupling parameter reflects the structural connectivity between two zones. However, a single Kuramoto oscillator has constant amplitude in complex domain, which makes comparison with real brain imaging data a challenging task. To overcome this, we introduce a hierarchical extension of the Kuramoto model with multiple nodes which may correspond to a recording from a single brain area or electrode. This allows for the representation of local synchronization within nodes and inter-areal interactions across nodes. Each node comprises multiple oscillators, whose behavior can be described by three key components:

$\frac{\delta\phi_i^n}{\delta t} = Natural + Internal + External + Noise$

Where $Natural = w_i^n$ represents the central frequency of the i-th oscillator in the n-th node and ϕ_i^n is the phase of the i-th oscillator in the n-th node,

$Internal = \frac{K_n}{N}\sum_{j=1}^{N} sin(\phi_i^n - \phi_j^n)$

where K_n is the local coupling parameter of the n-th node and N is the total number of oscillators within the node. In this context, the phase of each oscillator is shifted towards the average phase difference with the oscillators in the same node,

$External = \sum_{j=1}^{k} L_{n,j} * W_{n,j} * sin(\phi_i^n - \Phi_j) * R_j$

Where $L_{n,j}$ is the coupling coefficient between the n-th and j-th nodes (global control parameter), $W_{n,j}$ is the structural connectivity between the n-th and j-th nodes, Φ_j is the cyclic average of the phases of the n-th node defined as $\Phi_j = arg(\frac{1}{N}\sum_{q=1}^{N} e^{i\phi_q^j})$ and R_j is the order of the j-th node (see the definition below). In this context, the phase of each oscillator is compared to the average phase of other nodes and weighted by a node order and structural connectivity.

and $Noise = \eta_i^n$ is the white noise for the i-th oscillator in the n-th node.

At the final step, we computed the signal for each node by averaging the complex values of all oscillators, and the analytical time series of the n-th node is defined as $S_n = \frac{1}{N}\sum_j = 1^N e^{i*\phi_j^n}$. Thus, one is able to match a model's node to a single brain area or any other source of LFP recordings.

To improve computational performance, we use a complex-value representation for oscillator states. Thus, the coupling function between oscillators x and y becomes $imag(x * y^*)$, where x and y are complex values representing an oscillator phase, and y^* is a conjugate of y.

A. Computational experiments. For all experiments, each model node contained 1000 oscillators to ensure sufficient granularity in capturing local dynamics. In experiments for figures 2,3,4, oscillator frequencies were sampled from a normal distribution, centered at each node's central frequency (10 Hz), with a standard deviation of 1 Hz. As the noise component, we used normally distributed random values with a mean of 0 and a scale of 3 in all experiments.

We simulated 6 minutes of resting-state activity varying local and global control parameters, in experiments for figures 2,3 and 4 the K and L had equally spaced values from 0 to 8, in experiment for figure 5 the local coupling was varied from 0 to 20 and global coupling from 0 to 40. We cutoff the first minute of simulation to avoit the warmup period which inflates the DFA exponent values.

Observables of oscillatory dynamics. The order parameter is a key observable in the Kuramoto model, which quantifies the synchrony among oscillators within a node.. It is defined as the absolute value of the average complex-valued phase across oscillators that belong to the same node:

$R = |\frac{1}{N}\sum_{i=1}^{N} e^{i*\theta_i}|$

Where N is the number of oscillators and θ_i is the phase of the i-th oscillator.

To estimate inter-areal phase interactions, we computed phase synchrony metrics for each pair of nodes (in the model data) or parcels (in the MEG data). For the model, we used the phase locking value (PLV), defined as the absolute value of the complex PLV:

$cPLV = E[CS_{x,y}]$

Where E[.] denotes the expected value and $CS_{x,y}$ denotes the cross-spectrum between a complex signals X and Y. In practice, cPLV is estimated using limited data and sample cPLV is defined as

$\overline{cPLV}_{sample} = \frac{1}{N}\sum_{i=1}^{N} CS_{x,y}$

where N is the total number of samples.

For MEG data, we employed the weighted Phase Lag Index (wPLI), a metric robust to spurious zero-lag interactions, defined as:

$$wPLI = \frac{|\sum_{i=0}^{N} imag(CS_{x,y})|}{\sum_{i=0}^{N} |imag(CS_{x,y})|}$$

where $imag(CS_{x,y})$ is the imaginary part of the cross-spectrum of the complex time series x and y (77, 78).

The correlation coefficient between node time series is another way of estimating bivariate relations in a system. To include them in the analysis, we computed the Pearson correlation coefficient between each pair of model node order time series.

To measure long-range temporal correlations (LRTCs) in the model and MEG recordings, we used Detrended Fluctuation Analysis (DFA, (79)), which we computed in the Fourier domain to speed up the estimation (80). To obtain the DFA exponents from model or MEG data, we fitted the fluctuations as a function of window sizes using robust linear regression (81) with a bisquare weight function. We used 30 equally log-spaced windows, with sizes ranging from 10 central frequency cycles to 25% of the data.

Measures of similarity between observables of simulated and real data. We employed the Pearson correlation coefficient to quantify the similarity between observables of oscillatory dynamics derived from simulated and MEG data. For univariate node-level observables such as DFA and pACF, we computed the correlation coefficient between vectors of values for each parcel. For bivariate observables such as Phase Synchrony and Cross-Correlation matrices, we computed the correlation between values from the upper triangle of the matrix.

Code availability. The model code will be open-sourced following publication.

Data acquisition. Fifteen minutes eyes-open resting-state data were recorded from 20 healthy controls with 306-channel MEG (TRIUX, MEGIN Oy, Helsinki, Finland; 204 planar gradiometers and 102 magnetometers) at BioMag Laboratory, HUS Medical Imaging Center, Helsinki, Finland and 306-channel MEG (TRIUX neo, MEGIN Oy, Helsinki, Finland; 204 planar gradiometers and 102 magnetometers) at MEG Core, Aalto University, Espoo, Finland. Bipolar horizontal and vertical electrooculography (EOG) and electrocardiography (ECG) were also recorded. Participants were instructed to sit as still as possible and keep their eyes open to

DRAFT

focus on a cross displayed at the center of the screen in front of them.

T1-weighted anatomical magnetic resonance imaging (MRI) and diffusion weighted imaging (DWI) scans were obtained with a 3 Tesla whole-body MRI scanner (Magnetom Skyra, Siemens, Munich, Germany) at AMI Centre, Aalto University using a 32-channel head coil. T1-weighted MRI data were recorded with a resolution of 0.8×0.8×0.8 mm, repetition time of 2530 ms, and echo time of 3.42 ms. DWI data were recorded with a resolution of 3.0×3.0×3.0 mm, repetition time of 4100 ms, and echo time of 105 ms.

The study protocol for MEG, MRI, and DWI data was approved by the HUS ethical committee (**HUS/3043/2021**, 27.4.2022), written informed consent was obtained from each participant prior to the experiment, and all research was carried out according to the Declaration of Helsinki.

MEG data preprocessing and source modeling. Data preprocessing and source modeling were performed using the MNE software package (https://mne.tools/stable/index.html). Temporal signal space separation (tSSS) in the Maxfilter software (Elekta Neuromag Ltd., Finland) was used to suppress extracranial noise from MEG sensors, interpolate bad channels, and compensate for head motions. Independent components analysis was used to identify and remove components that were correlated with ocular (using the EOG signal), heart-beat (using the magnetometer signal as reference), or muscle artefacts.

We used the FreeSurfer 7.3.2 software (https://surfer.nmr.mgh.harvard.edu/) for volumetric segmentation of MRI data, surface reconstruction, flattening, and cortical parcellation. Source reconstruction was performed with minimum norm estimation (MNE) using dynamic statistical parametric maps (dSPM). A surface-based source space with 5 mm spacing and 1 layer (inner skull) symmetric boundary element method (BEM) was used in computing the forward operator, and noise covariance matrices were obtained from preprocessed data filtered to 151-249 Hz. We then estimated vertex fidelity to obtain fidelity-weighted inverse operators to reduce the effects of spurious connections resulting from source leakage and collapsed the inverse-transformed source time series into parcel time series in a manner that maximizes the source-reconstruction accuracy (82, 83). Source time series were collapsed to the 200 parcels of the Schaefer atlas (84).

In this study, we used complex Morlet wavelets to obtain a narrow-band representation of a MEG signal (85). 50 Hz line-noise and it's harmonics were suppressed with a notch filter with 1 Hz band transition widths. The band-pass (1-249 Hz) filtered data were then separated into narrow frequency bands with 41 equally log-spaced Morlet wavelets with frequencies ranging from 1 Hz to 100 Hz (number of cycles in a Morlet Wavelet = 5.0).

DWI data preprocessing. The DWI data preprocessing, including denoising and motion correction, was conducted using the MRtrix3 3.0.1 Toolbox (86) and FMRIB Software Library (FSL) 6.0.5 (87). To lessen potential biases or artifacts arising during image acquisition or processing, the Advanced Normalization Tools (ANTs) 2.3.5 was used (88). For T1-weighted anatomical MRI data preprocessing, creation of head models and cortical surface reconstruction, we used the open-source FreeSurfer 7.3.2 software (available at https://surfer.nmr.mgh.harvard.edu/, (89)). In the subsequent step, Constrained Spherical Deconvolution (CSD) (90) was employed to determine the fiber orientation distributions (FODs) within each voxel, allowing for the accurate decomposition of the diffusion signal into individual fiber orientations. In order to improve the accuracy of fiber tracking, anatomically-constrained tractography (ACT, (91)) was also applied by incorporating anatomical information through the five-tissue-type (5TT) segmentation derived from diverse brain tissues. The resulting FODs provided a detailed map of white matter tracts. For tractography construction, the principal diffusion direction was obtained from each of the 20 000 000 seed points. To refine the quality of the diffusion image and minimize tractogram reconstruction biases, we applied the Spherical informed filtering of tractograms approach (SIFT2, (92)).

T1-weighted anatomical MRI and DWI coregistration was performed using the Spm 12 package within MATLAB R2022a software. All preprocessing steps were executed on the CentOS Linux operating system, operating on the Triton high-performance computing cluster at Aalto University.

Following preprocessing, structural connectomes (SCs) were constructed as edge-adjacency matrices representing the count of white matter connections between parcelled cortical and subcortical brain regions. The resulting matrices are symmetric, reflecting undirected pairwise connections between brain regions (nodes). The nodes correspond to the 200 parcels of the Schaefer atlas (84), matched with Yeo 17 networks (93).

ACKNOWLEDGMENTS. We thank Sheng Wang, Felix Siebenhühner and Joonas J. Juvonen for feedback about the study. We also thank professor Guido Nolte on helpful comments on an earlier version of the manuscript. This study was supported by the Academy of Finland (J.M.P., project numbers: 296304), by the Juselius Foundation (S.P and J.M.P project number 240156).

DRAFT

1. G Arnulfo, J Hirvonen, L Nobili, S Palva, JM Palva, Phase and amplitude correlations in resting-state activity in human stereotactical eeg recordings. *NeuroImage* **112**, 114–127 (2015).
2. G Arnulfo, et al., Long-range phase synchronization of high-frequency oscillations in human cortex. *Nat. Commun.* **11** (2020).
3. N Williams, et al., The influence of inter-regional delays in generating large-scale brain networks of phase synchronization. *NeuroImage* **279**, 120318 (2023).
4. S Palva, JM Palva, Discovering oscillatory interaction networks with m/eeg: challenges and breakthroughs. *Trends Cogn. Sci.* **16**, 219–230 (2012).
5. MJ Brookes, et al., Investigating the electrophysiological basis of resting state networks using magnetoencephalography. *Proc. Natl. Acad. Sci.* **108**, 16783–16788 (2011).
6. M Siems, AA Pape, JF Hipp, M Siegel, Measuring the cortical correlation structure of spontaneous oscillatory activity with eeg and meg. *NeuroImage* **129**, 345–355 (2016).
7. P Fries, Rhythms for cognition: Communication through coherence. *Neuron* **88**, 220–235 (2015).
8. M Vinck, et al., Principles of large-scale neural interactions. *Neuron* **111**, 987–1002 (2023).
9. M Schneider, et al., A mechanism for inter-areal coherence through communication based on connectivity and oscillatory power. *Neuron* **109**, 4050–4067.e12 (2021).
10. JM Palva, S Monto, S Kulashekhar, S Palva, Neuronal synchrony reveals working memory networks and predicts individual memory capacity. *Proc. Natl. Acad. Sci.* **107**, 7580–7585 (2010).
11. H Haque, M Lobier, JM Palva, S Palva, Neuronal correlates of full and partial visual conscious perception. *Conscious. Cogn.* **78**, 102863 (2020).
12. F Siebenhühner, SH Wang, JM Palva, S Palva, Cross-frequency synchronization connects networks of fast and slow oscillations during visual working memory maintenance. *eLife* **5** (2016).
13. SH Wang, et al., Neuronal synchrony and critical bistability: Mechanistic biomarkers for localizing the epileptogenic network. *preprint* (2023).
14. LI Boon, et al., A systematic review of meg-based studies in parkinson's disease: The motor system and beyond. *Hum. Brain Mapp.* **40**, 2827–2848 (2019).
15. S Pusil, et al., Hypersynchronization in mild cognitive impairment: the 'x'model. *Brain* **142**, 3936–3950 (2019).
16. G Alamian, et al., Alterations of intrinsic brain connectivity patterns in depression and bipolar disorders: A critical assessment of magnetoencephalography-based evidence. *Front. Psychiatry* **8** (2017).
17. S Zhang, et al., Association between abnormal default mode network activity and suicidality in depressed adolescents. *BMC Psychiatry* **16** (2016).
18. RH Kaiser, JR Andrews-Hanna, TD Wager, DA Pizzagalli, Large-scale network dysfunction in major depressive disorder: A meta-analysis of resting-state functional connectivity. *JAMA Psychiatry* **72**, 603 (2015).
19. Y Mohammadi, MH Moradi, Prediction of depression severity scores based on functional connectivity and complexity of the eeg signal. *Clin. EEG Neurosci.* **52**, 52–60 (2020).
20. G Buzsáki, CA Anastassiou, C Koch, The origin of extracellular fields and currents–EEG, ECoG, LFP and spikes. *Nat. Rev. Neurosci.* **13**, 407–420 (2012).
21. S Palva, S Monto, JM Palva, Graph properties of synchronized cortical networks during visual working memory maintenance. *NeuroImage* **49**, 3257–3268 (2010).
22. J Simola, et al., Genetic polymorphisms in comt and bdnf influence synchronization dynamics of human neuronal oscillations. *iScience* **25**, 104985 (2022).
23. C Micou, T O'Leary, Representational drift as a window into neural and behavioural plasticity. *Curr. Opin. Neurobiol.* **81**, 102746 (2023).
24. WL Shew, D Plenz, The functional benefits of criticality in the cortex. *The Neurosci.* **19**, 88–100 (2012).
25. DR Chialvo, Emergent complex neural dynamics. *Nat. Phys.* **6**, 744–750 (2010).
26. K Linkenkaer-Hansen, VV Nikouline, JM Palva, RJ Ilmoniemi, Long-range temporal correlations and scaling behavior in human brain oscillations. *The J. Neurosci.* **21**, 1370–1377 (2001).
27. JM Beggs, D Plenz, Neuronal avalanches in neocortical circuits. *The J. Neurosci.* **23**, 11167–11177 (2003).

28. N Lotfi, et al., Statistical complexity is maximized close to criticality in cortical dynamics. *Phys. Rev. E* **103** (2021).
29. O Kinouchi, M Copelli, Optimal dynamical range of excitable networks at criticality. *Nat. Phys.* **2**, 348–351 (2006).
30. V Zimmern, Why brain criticality is clinically relevant: A scoping review. *Front. Neural Circuits* **14** (2020).
31. K Heiney, et al., Criticality, connectivity, and neural disorder: A multifaceted approach to neural computation. *Front. Comput. Neurosci.* **15** (2021).
32. JM Beggs, The criticality hypothesis: how local cortical networks might optimize information processing. *Philos. Transactions Royal Soc. A: Math. Phys. Eng. Sci.* **366**, 329–343 (2007).
33. JM Shine, et al., Computational models link cellular mechanisms of neuromodulation to large-scale neural dynamics. *Nat. Neurosci.* **24**, 765–776 (2021).
34. JM Shine, Neuromodulatory control of complex adaptive dynamics in the brain. *Interface Focus.* **13** (2023).
35. JM Beggs, N Timme, Being critical of criticality in the brain. *Front. physiology* **3**, 163 (2012).
36. M Rubinov, O Sporns, JP Thivierge, M Breakspear, Neurobiologically realistic determinants of self-organized criticality in networks of spiking neurons. *PLoS Comput. Biol.* **7**, e1002038 (2011).
37. SJ Wang, C Zhou, Hierarchical modular structure enhances the robustness of self-organized criticality in neural networks. *New J. Phys.* **14**, 023005 (2012).
38. G Ódor, R Dickman, G Ódor, Griffiths phases and localization in hierarchical modular networks. *Sci. Reports* **5** (2015).
39. SS Poil, R Hardstone, HD Mansvelder, K Linkenkaer-Hansen, Critical-state dynamics of avalanches and oscillations jointly emerge from balanced excitation/inhibition in neuronal networks. *J. Neurosci.* **32**, 9817–9823 (2012).
40. M Fuscà, et al., Brain criticality predicts individual levels of inter-areal synchronization in human electrophysiological data. *Nat. Commun.* **14** (2023).
41. JM Palva, et al., Neuronal long-range temporal correlations and avalanche dynamics are correlated with behavioral scaling laws. *Proc. Natl. Acad. Sci.* **110**, 3585–3590 (2013).
42. P Ritter, M Schirner, AR McIntosh, VK Jirsa, The virtual brain integrates computational modeling and multimodal neuroimaging. *Brain Connect.* **3**, 121–145 (2013).
43. A Ponce-Alvarez, G Deco, The hopf whole-brain model and its linear approximation. *Sci. Reports* **14** (2024).
44. M Breakspear, S Heitmann, A Daffertshofer, Generative models of cortical oscillations: neurobiological implications of the kuramoto model. *Front. human neuroscience* **4**, 190 (2010).
45. J Cabral, et al., Metastable oscillatory modes emerge from synchronization in the brain spacetime connectome. *Commun. Phys.* **5** (2022).
46. R Schmidt, et al., Beta oscillations in working memory, executive control of movement and thought, and sensorimotor function. *The J. Neurosci.* **39**, 8231–8238 (2019).
47. JC Pang, LL Gollo, JA Roberts, Stochastic synchronization of dynamics on the human connectome. *NeuroImage* **229**, 117738 (2021).
48. F Siebenhühner, et al., Genuine cross-frequency coupling networks in human resting-state electrophysiological recordings. *PLOS Biol.* **18**, e3000685 (2020).
49. JP Hobbs, JL Smith, JM Beggs, Aberrant neuronal avalanches in cortical tissue removed from juvenile epilepsy patients. *J. Clin. Neurophysiol.* **27**, 380–386 (2010).
50. Y Liu, KA Dahmen, Unexpected universality in static and dynamic avalanches. *Phys. Rev. E* **79** (2009).
51. MJ Aburn, CA Holmes, JA Roberts, TW Boonstra, M Breakspear, Critical fluctuations in cortical models near instability. *Front. Physiol.* **3** (2012).
52. G Deco, ML Kringelbach, VK Jirsa, P Ritter, The dynamics of resting fluctuations in the brain: metastability and its dynamical cortical core. *Sci. Reports* **7** (2017).
53. JA Roberts, et al., Metastable brain waves. *Nat. Commun.* **10** (2019).
54. AE Avramiea, A Masood, HD Mansvelder, K Linkenkaer-Hansen, Long-range amplitude coupling is optimized for brain networks that function at criticality. *J. Neurosci.* **42**, 2221–2233 (2022).
55. L Dalla Porta, M Copelli, Modeling neuronal avalanches and long-range temporal correlations at the emergence of collective oscillations: Continuously varying exponents mimic m/eeg results. *PLOS Comput. Biol.* **15**, e1006924 (2019).
56. P Villegas, P Moretti, MA Muñoz, Frustrated hierarchical synchronization and emergent complexity in the human connectome network. *Sci. Reports* **4** (2014).
57. DP Koller, M Schirner, P Ritter, Human connectome topology directs cortical traveling waves and shapes frequency gradients. *Nat. Commun.* **15** (2024).
58. A Escrichs, et al., Whole-brain turbulent dynamics predict responsiveness to pharmacological treatment in major depressive disorder. *Mol. Psychiatry* (2024).
59. SH Wang, et al., Critical-like brain dynamics in a continuum from second- to first-order phase transition. *The J. Neurosci.* **43**, 7642–7656 (2023).
60. S Kuroki, K Mizuseki, Excitation–inhibition balance controls synchronization in a simple model of coupled phase oscillators. *preprint* (2024).
61. Y Kuramoto, International symposium on mathematical problems in theoretical physics. *Lect. notes Phys.* **30**, 420 (1975).
62. T Donoghue, et al., Parameterizing neural power spectra into periodic and aperiodic components. *Nat. Neurosci.* **23**, 1655–1665 (2020).
63. V Myrov, et al., Rhythmicity of neuronal oscillations delineates their cortical and spectral architecture. *Commun. Biol.* **7** (2024).
64. JD Cowan, J Neuman, W van Drongelen, Wilson–cowan equations for neocortical dynamics. *The J. Math. Neurosci.* **6** (2016).
65. K Linkenkaer-Hansen, VV Nikouline, JM Palva, RJ Ilmoniemi, Long-range temporal correlations and scaling behavior in human brain oscillations. *J. Neurosci.* **21**, 1370–1377 (2001).
66. A Zhigalov, G Arnulfo, L Nobili, S Palva, JM Palva, Relationship of fast- and slow-timescale neuronal dynamics in human meg and seeg. *The J. Neurosci.* **35**, 5385–5396 (2015).
67. O Shriki, et al., Neuronal avalanches in the resting meg of the human brain. *The J. Neurosci.* **33**, 7079–7090 (2013).
68. F Dorfler, F Bullo, On the critical coupling for kuramoto oscillators (2011).
69. G Ódor, J Kelling, Critical synchronization dynamics of the kuramoto model on connectome and small world graphs. *Sci. reports* **9**, 19621 (2019).
70. G Ódor, B de Simoni, Heterogeneous excitable systems exhibit griffiths phases below hybrid phase transitions. *Phys. Rev. Res.* **3**, 013106 (2021).
71. A Haimovici, P Balenzuela, E Tagliazucchi, Dynamical signatures of structural connectivity damage to a model of the brain posed at criticality. *Brain Connect.* **6**, 759–771 (2016).
72. H Markram, et al., Reconstruction and simulation of neocortical microcircuitry. *Cell* **163**, 456–492 (2015).
73. A Haimovici, E Tagliazucchi, P Balenzuela, DR Chialvo, Brain organization into resting state networks emerges at criticality on a model of the human connectome. *Phys. Rev. Lett.* **110**, 178101 (2013).
74. RP Rocha, et al., Recovery of neural dynamics criticality in personalized whole-brain models of stroke. *Nat. Commun.* **13** (2022).
75. G Deco, et al., Rare long-range cortical connections enhance human information processing. *Curr. Biol.* **31**, 4436–4448.e5 (2021).
76. R Sanchez-Todo, et al., A physical neural mass model framework for the analysis of oscillatory generators from laminar electrophysiological recordings. *NeuroImage* **270**, 119938 (2023).
77. SH Wang, et al., Hyperedge bundling: A practical solution to spurious interactions in MEG/EEG source connectivity analyses. *NeuroImage* **173**, 610–622 (2018).
78. M Vinck, R Oostenveld, M van Wingerden, F Battaglia, CM Pennartz, An improved index of phase-synchronization for electrophysiological data in the presence of volume-conduction, noise and sample-size bias. *NeuroImage* **55**, 1548–1565 (2011).
79. R Hardstone, et al., Detrended fluctuation analysis: a scale-free view on neuronal oscillations. *Front. physiology* **3**, 450 (2012).
80. G Nolte, M Aburidi, AK Engel, Robust calculation of slopes in detrended fluctuation analysis and its application to envelopes of human alpha rhythms. *Sci. Reports* **9** (2019).
81. PJ Huber, Robust regression: Asymptotics, conjectures and monte carlo. *The Annals Stat.* **1** (1973).
82. O Korhonen, S Palva, JM Palva, Sparse weightings for collapsing inverse solutions to cortical parcellations optimize m/EEG source reconstruction accuracy. *J. Neurosci. Methods* **226**, 147–160 (2014).
83. F Siebenhühner, et al., Genuine cross-frequency coupling networks in human resting-state electrophysiological recordings. *PLOS Biol.* **18**, e3000685 (2020).
84. A Schaefer, et al., Local-global parcellation of the human cerebral cortex from intrinsic functional connectivity mri. *Cereb. cortex* **28**, 3095–3114 (2018).
85. MX Cohen, A better way to define and describe morlet wavelets for time-frequency analysis. *NeuroImage* **199**, 81–86 (2019).
86. JD Tournier, et al., Mrtrix3: A fast, flexible and open software framework for medical image processing and visualisation. *NeuroImage* **202**, 116137 (2019).
87. M Jenkinson, CF Beckmann, TE Behrens, MW Woolrich, SM Smith, Fsl. *NeuroImage* **62**, 782–790 (2012).
88. BB Avants, N Tustison, G Song, , et al., Advanced normalization tools (ants). *Insight j* **2**, 1–35 (2009).
89. B Fischl, Freesurfer. *NeuroImage* **62**, 774–781 (2012).
90. JD Tournier, F Calamante, A Connelly, Robust determination of the fibre orientation distribution in diffusion mri: non-negativity constrained super-resolved spherical deconvolution. *Neuroimage* **35**, 1459–1472 (2007).
91. RE Smith, JD Tournier, F Calamante, A Connelly, Anatomically-constrained tractography: improved diffusion mri streamlines tractography through effective use of anatomical information. *Neuroimage* **62**, 1924–1938 (2012).
92. RE Smith, JD Tournier, F Calamante, A Connelly, Sift: Spherical-deconvolution informed filtering of tractograms. *Neuroimage* **67**, 298–312 (2013).
93. BT Yeo, et al., The organization of the human cerebral cortex estimated by intrinsic functional connectivity. *J. neurophysiology* (2011).

DRAFT